



Cite this: *Chem. Sci.*, 2024, 15, 4341 All publication charges for this article have been paid for by the Royal Society of Chemistry

# A covalent organic framework as a dual-active-center cathode for a high-performance aqueous zinc-ion battery†

Hongbao Li,<sup>‡</sup> Mengge Cao,<sup>‡</sup> Zhenli Fu,<sup>‡</sup> Quanwei Ma, Longhai Zhang, Rui Wang, Fei Liang, Tengfei Zhou  and Chaofeng Zhang \*

Organic electrode materials have shown significant potential for aqueous Zn ion batteries (AZIBs) due to their flexible structure designability and cost advantage. However, sluggish ionic diffusion, high solubility, and low capacities limit their practical application. Here, we designed a covalent organic framework (TA-PTO-COF) generated by covalently bonding tris(4-formylbiphenyl)amine (TA) and 2,7-diaminopyrene-4,5,9,10-tetraone (PTO-NH<sub>2</sub>). The highly conjugated skeleton inside enhances its electron delocalization and intermolecular interaction, leading to high electronic conductivity and limited solubility. The open channel within the TA-PTO-COF provides ionic diffusion pathways for fast reaction kinetics. In addition, the abundant active sites (C=N and C=O) endow the TA-PTO-COF with a large reversible capacity. As a result, the well-designed TA-PTO-COF cathode delivers exceptional capacity (255 mA h g<sup>-1</sup> at 0.1 A g<sup>-1</sup>), excellent cycling stability, and a superior rate capacity of 186 mA h g<sup>-1</sup> at 10 A g<sup>-1</sup>. Additionally, the co-insertion mechanism of Zn<sup>2+</sup>/H<sup>+</sup> within the TA-PTO-COF cathode is revealed in depth by *ex situ* spectroscopy. This study presents an effective strategy for developing high-performance organic cathodes for advanced AZIBs.

Received 31st December 2023  
Accepted 26th January 2024

DOI: 10.1039/d3sc07013a

rsc.li/chemical-science

## Introduction

The exploration of advanced and eco-friendly electrochemical energy storage systems was prompted by the energy crisis and environmental pollution.<sup>1–5</sup> One of the most promising candidates for next-generation large-scale energy storage is rechargeable aqueous metal-ion batteries, which feature high safety, low cost, and environmental friendliness.<sup>6–10</sup> Different from organic solvent-based electrolytes, aqueous electrolytes possess high ionic conductivity, low toxicity, and non-flammability.<sup>11,12</sup> Among them, AZIBs are desirable energy storage devices due to the inherent merits of affordable and non-toxic zinc, which is found in high abundance in nature (300 times higher than lithium), possesses a low redox potential of –0.76 V and has a large theoretical capacity of 820 mA h g<sup>-1</sup>.<sup>13–17</sup> Up to now, various inorganic cathode materials have been explored to achieve high energy densities and good stability, such as manganese-based and vanadium-based materials, and Prussian

blue analogues.<sup>18–20</sup> However, they suffer from poor cycling performance owing to their dissolution in acidic electrolyte, and their structure variation during repeating charge/discharge processes. Furthermore, the scarcity of transition metal elements will result in high cost and impede the large-scale application of AZIBs.<sup>21</sup>

Organic compounds are composed primarily of naturally occurring elements, including C, H, N, O, and S elements. These compounds possess many advantages in terms of low cost, structural diversity, design flexibility, and meeting the requirements for sustainable development.<sup>1,8,22,23</sup> Importantly, the structural diversity of organic compounds contributes to easy tailoring of their electrochemical performance on the molecular level, leading to a large number of new types of organic cathodes.<sup>24–29</sup> In addition, the unique reaction mechanism and flexible structure of organic compounds can avoid large structural changes and enhance the mobility of large-sized Zn ions, which is vital for the operation of high-performance AZIBs.<sup>30</sup> To date, many organic electrodes have been discovered, such as conductive polymers, organosulfur compounds, and nitroxide radical and carbonyl group-containing compounds.<sup>27,31,32</sup> In particular, carbonyl compounds have achieved significant success as cathodes for rechargeable metal-ion batteries.<sup>33</sup> However, the high solubility and low conductivity of small organic molecules greatly restrict their cyclability and rate performance. To solve these problems, salification, hybridization, and polymerization have been adopted. However, the

*Institutes of Physical Science and Information Technology, Leibniz International Joint Research Center of Materials Sciences of Anhui Province, Anhui Province Key Laboratory of Environment-Friendly Polymer Materials, Key Laboratory of Structure and Functional Regulation of Hybrid Material (Ministry of Education), Anhui University, Hefei 230601, China. E-mail: cfz@ahu.edu.cn*

† Electronic supplementary information (ESI) available. See DOI: <https://doi.org/10.1039/d3sc07013a>

‡ These authors contributed equally to this work.



introduced inactive composition and dense structure of the polymer will inevitably lead to reduced capacity and low ionic conductivity.<sup>25</sup> Therefore, it is essential and challenging to design carbonyl compounds with high ionic/electronic conductivity, multiple electroactive centers, and excellent chemical/physical stability.<sup>34</sup>

Covalent organic frameworks (COFs) are a class of porous crystalline organic materials constructed from covalently linked and periodically arranged organic molecules.<sup>35–37</sup> Benefitting from their highly cross-linked frameworks, robust covalent bond, and strong  $\pi$ - $\pi$  stacking interactions, COFs exhibit stable chemical and physical characteristics and are resistant to solubility problems in organic electrolytes.<sup>38,39</sup> Notably, unlike the dense structure of polymers, the open pore channels in the COFs provide sufficient diffusion pathways for metal ions to access the active sites inside, thereby resulting in high active site utilization.<sup>40</sup> Additionally, the redox-active units within the COFs can be precisely manipulated at the molecular level, resulting in a large capacity.<sup>41</sup> COFs are promising electrode materials for rechargeable AZIBs due to their unique properties. However, most of the COF electrodes contain only a single active redox group, which inevitably leads to a low theoretical and practical capacity.<sup>42,43</sup>

Herein, we designed and synthesized a covalent organic framework (TA-PTO-COF) with the dual redox-active sites of C=O and C=N *via* bonding tris(4-formylbiphenyl)amine (TA) and 2,7-diaminopyrene-4,5,9,10-tetraone (PTO-NH<sub>2</sub>). The conjugated structure, multiple active sites (C=N and C=O groups) and regular channels endowed TA-PTO-COF with high conductivity, plentiful exposed active sites, and fast ion diffusion pathways, resulting in rapid reaction kinetics and large capacity. In addition, the large molecular structure, robust covalent framework, and conjugated structure-induced  $\pi$ - $\pi$  stacking inhibit solubility in the electrolyte and improve the structural stability. TA-PTO-COF as a cathode material showed a high discharge capacity of 255 mA h g<sup>-1</sup> at 0.1 A g<sup>-1</sup>, exceptional rate performance (186 mA h g<sup>-1</sup> at 10 A g<sup>-1</sup>) and long-term cyclability (1000 cycles at 1 A g<sup>-1</sup>). Importantly, the Zn<sup>2+</sup>/H<sup>+</sup> co-insertion behavior within TA-PTO-COF was confirmed in detail through *ex situ* measurements. This study presents an organic cathode material for AZIBs and offers new insights into the development of COFs for the next generation of batteries.<sup>44</sup>

## Experimental section

### Synthesis of monomeric pyrene-4,5,9,10-tetrone (PTO)

First, a solution of pyrene (4.0 g) was prepared by dissolving it in a mixture of dichloromethane (140 mL) and acetonitrile (140 mL) in a round-bottom flask. After the pyrene was completely dissolved, the mixture of 70.0 g of sodium periodate and 200 mL of deionized water was stirred at 35 °C for 10 h after adding 1.0 g of ruthenium(III) chloride hydrate. After the reaction, the black-green precipitate was removed by filtration and washed repeatedly with a large amount of dichloromethane to remove any remaining impurities. The yellow filtrate was extracted with dichloromethane to eliminate any residual small amount of black-green suspension, and finally, the resulting yellow

organic solution was purified using column chromatography to remove by-products and obtain an orange product. The yield of PTO was 23.2%. <sup>1</sup>H NMR (400 MHz, DMSO-*d*<sub>6</sub>, 298 K),  $\delta$  8.33 (d, *J* = 7.7 Hz, 4H), 7.74 (t, *J* = 7.7 Hz, 2H).

### Synthesis of 2,7-dinitropyrene-4,5,9,10-tetrone (PTO-NO<sub>2</sub>)

PTO (4.73 mmol, 1.24 g) was added to a mixture of sulfuric acid and nitric acid (4 : 1 by volume) and the solution was then refluxed at 90 °C for 4 h. Following the reaction, the mixture was poured into 200 mL of deionized water. The mixture was then filtered multiple times with saturated sodium bicarbonate and water. The resulting yellow precipitate was collected and dried under vacuum at 65 °C for 24 h, yielding 1.32 g of yellow PTO-NO<sub>2</sub> in 75% yield. <sup>1</sup>H NMR (400 MHz, DMSO-*d*<sub>6</sub>, 298 K),  $\delta$  8.89 (d, *J* = 7.7 Hz, 4H).

### Synthesis of 2,7-diaminopyrene-4,5,9,10-tetraone (PTO-NH<sub>2</sub>)

PTO-NO<sub>2</sub> (2 mmol, 704 mg) and Na<sub>2</sub>S 9H<sub>2</sub>O (24 mmol, 5.76 g) were first added to 60 mL DMF, and the mixture was reacted at 80 °C for 10 h under an argon atmosphere. Then, the product was poured into 100 mL of ethyl acetate, and the sample was filtered and washed with methanol and water, and then dried under vacuum at 65 °C for 24 h, resulting in a purple-black powder. The crude product was further purified by dispersing it in 20 mL of carbon disulfide and then heating it in an oven to yield black PTO-NH<sub>2</sub> weighing 314 mg (70% yield). <sup>1</sup>H NMR (400 MHz, DMSO-*d*<sub>6</sub>, 298 K),  $\delta$  7.37 (d, *J* = 7.7 Hz, 2H), 5.96 (t, *J* = 7.7 Hz, 2H).

### Synthesis of TA-PTO-COF

PTO-NH<sub>2</sub> (21.9 mg, 0.075 mmol) and tris(4-formylbiphenyl)amine (TA) (10.5 mg, 0.05 mmol) were added to a Schlenk tube, followed by the addition of 0.9 mL of homotrimethylbenzene, 0.3 mL 1,4-dioxane and 0.1 mL acetic acid. The tube was subsequently subjected to frozen degassing 3 times under an argon atmosphere, and at 120 °C for 3 days. Finally, the black powder of TA-PTO-COF (29 mg, 87%) was obtained by filtering, washing to separate, and drying.

### Material characterization

The chemical composition and structure of TA-PTO-COF were identified by Fourier transform infrared spectroscopy (FT-IR, Vertex80+Hyperion 2000), X-ray photoelectron spectroscopy (XPS, Axis Ultra DLD Kratos AXIS SUPRA), and powder X-ray diffractometry (PXRD, Bruker D8 Advance, Germany). The morphology was observed by scanning electron microscopy (SEM, Regulus 8230). Thermal stability was studied by thermogravimetric analysis (TGA, TG 209 F3 Tarsus) under nitrogen atmosphere.

### Electrochemical measurements

The working electrodes were composed of active materials, Ketjen black, and PVDF in a mass ratio of 6 : 3 : 1. The mass loading of the corresponding active components of the electrode was about 1.0–1.1 mg cm<sup>-2</sup>. TA-PTO-COF, zinc foil, and



2 M ZnSO<sub>4</sub> were used as the cathode, anode, and electrolyte, respectively. The amount of electrolyte (2 M ZnSO<sub>4</sub>) is 50 μL. The electrochemical performance of the assembled batteries was evaluated on NEWARE equipment and a CHI 760E electrochemical workstation.

### Theoretical calculations

The structure of TA-PTO-COF was constructed and optimized at the B3LYP/6-31+G (p) level. Then the repeated unit was selected and reoptimized at the same level. The corresponding highest occupied molecular orbitals (HOMO), the lowest unoccupied molecular orbitals (LUMO), and the electron density distribution were determined using the Multiwfn 3.8 program. The Gaussian 16 software package was used for all theoretical calculations.<sup>45</sup>

## Results and discussion

The synthesis of the PTO-NH<sub>2</sub> precursor is displayed in Scheme S1,† and the product of each step was confirmed by <sup>1</sup>H NMR (Fig. S1–S3†). TA-PTO-COF was synthesized through a Schiff-based reaction between TA and PTO-NH<sub>2</sub>. The electrolyte soaked with TA-PTO-COF is almost colorless, indicating the low solubility of TA-PTO-COF in the electrolyte (Fig. 1a). Additionally, further analysis of the UV-vis spectrum was conducted to confirm the solubility of TA-PTO-COF in electrolytes (Fig. S4†). It is evident that the presence of TA-PTO-COF in the electrolyte

produces a spectrum similar to that of the bare electrolyte, providing further confirmation of its insolubility. Density functional theory (DFT) calculations were applied to understand the electrochemical properties of TA-PTO-COF. As shown in Fig. 1b, the frontier molecular orbital calculations included the highest occupied molecular orbital (HOMO) and the lowest unoccupied molecular orbital (LUMO). TA-PTO-COF shows a low LUMO energy, which contributes to enhancing the charge delocalization. The narrow energy gap ( $\Delta E$ ) of 1.85 eV between the HOMO and LUMO of TA-PTO-COF indicates efficient electron conduction with low energy barriers, which facilitates better charge transfer and redox reaction.<sup>40</sup> The molecular electrostatic potential (MESP) was used to study the electronic structure and further elucidate the active sites of TA-PTO-COF. As shown in Fig. 1c, the positive MESP region is represented by the red region, which is the nucleophilic center, while the electrophilic center is represented by the blue region (negative MESP region).<sup>46</sup> The electronegativity of the TA-PTO-COF molecules is concentrated in the blue region surrounding the C=N and C=O groups, revealing the electrochemically active sites for storing the cations (such as Zn<sup>2+</sup> and H<sup>+</sup>). The PXRD pattern of TA-PTO-COF exhibits high crystallinity and typical peaks located at 6.50° and 28.62°, which correspond to the (110) and (001) planes, respectively, indicating the presence of a crystalline framework structure (Fig. 1d). Among them, the (001) plane is mainly attributed to the  $\pi$ - $\pi$  stacking between the layers of TA-PTO-COF,<sup>47</sup> indicating a multilayered COF

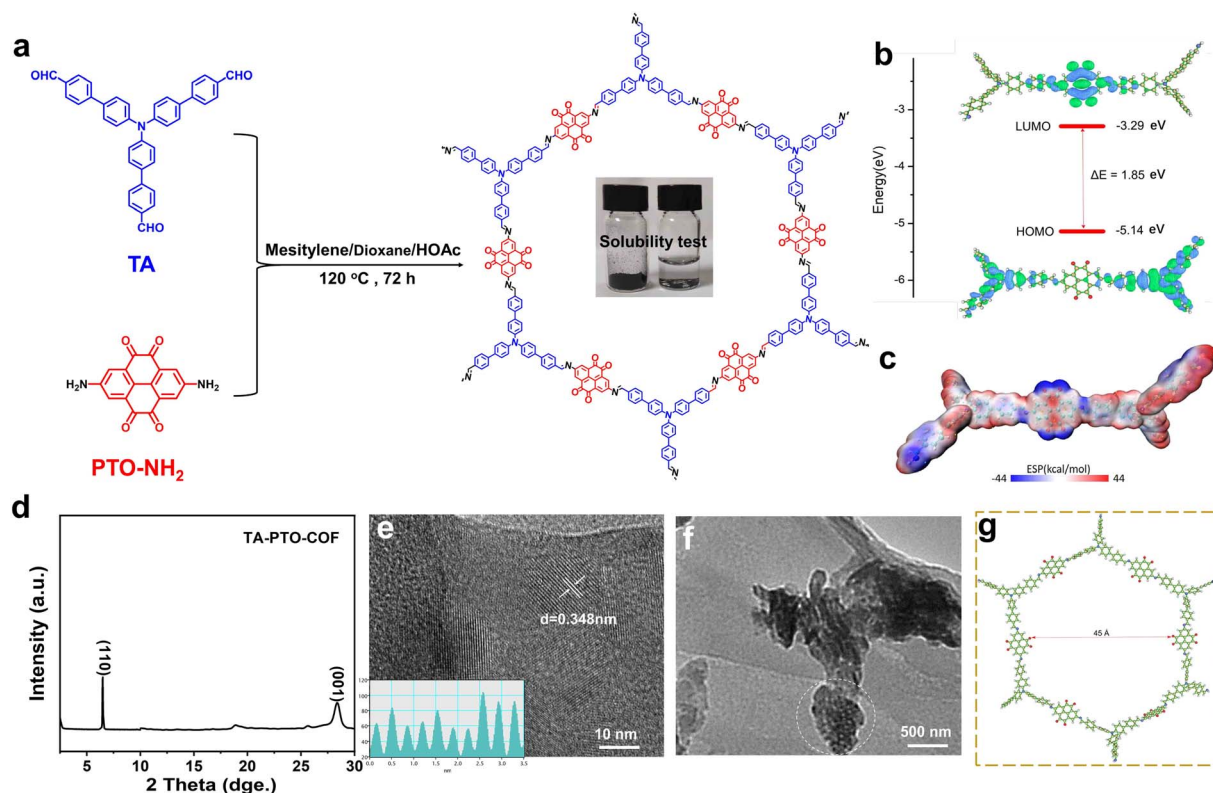


Fig. 1 (a) Illustration of the synthetic route for TA-PTO-COF. (b) Calculated frontier molecular orbital energy. (c) Calculated MESP distribution of TA-PTO-COF. (d) PXRD pattern of the TA-PTO-COF. (e and f) TEM images of TA-PTO-COF. (g) Calculated aperture size of TA-PTO-COF.





structure. The crystal structure of TA-PTO-COF was confirmed by transmission electron microscopy (TEM) and revealed that the lattice strip spacing of TA-PTO-COF is 0.348 nm, corresponding to the (001) facets (Fig. 1e).<sup>38</sup> Fig. 1f demonstrates that TA-PTO-COF possesses a pore structure (the area outlined in white), while Fig. 1g illustrates its typical mesoporous nature with a pore diameter of about 45 Å.

The chemical structure features of TA-PTO-COF were also investigated. Fig. 2a shows the Fourier transform infrared spectra (FT-IR) of PTO-NH<sub>2</sub>, TA, and TA-PTO-COF. Compared with the PTO-NH<sub>2</sub> monomer, TA-PTO-COF shows a weaker -NH<sub>2</sub> stretching vibration peak around 3500–3000 cm<sup>-1</sup>, indicating the presence of residual -NH<sub>2</sub> groups at the edge of TA-PTO-COF. The peak at 3078 cm<sup>-1</sup> corresponds to the C-H stretching vibration peak, and the peaks at 1673 and 1275 cm<sup>-1</sup> are assigned to the C=O and C-N bonds, respectively.<sup>48</sup> Specifically, a peak at 1452 cm<sup>-1</sup> emerges in the COF, which is primarily attributed to the vibration of C=N. These results prove the successful preparation of TA-PTO-COF. Additionally, the chemical composition of TA-PTO-COF was demonstrated by X-ray photoelectron spectroscopy (XPS). The survey spectra confirmed the presence of C, N, and O elements in TA-PTO-COF (Fig. 2b). As shown in Fig. 2c, the C 1s spectra at 287.5 eV, 284.8 eV, 286.41 eV, and 285.5 eV correspond to C=O, C-C/C=C, C=N, and C-N bonds, respectively. It should be noted that the  $\pi$ - $\pi^*$  peak at 291.3 eV can be observed which is mainly attributed to the  $\pi$ - $\pi$  stacking between the TA-PTO-COF layers. The N 1s spectra exhibit two distinct peaks at 399.6 and 400.5 eV, which correspond to the C=N and C-N bonds from the imine group and TA unit, respectively (Fig. 2d). This result is consistent with the findings of the C 1s spectra. Fig. 2e displays the energy-dispersive spectroscopy (EDS) elemental mapping images, which confirm the uniform distribution of C, N, and O

elements. Fig. 2f shows the thermal stability of TA-PTO-COF quantified by thermogravimetric analysis (TGA), demonstrating thermal stability up to 311 °C in nitrogen.

To optimize the electrochemical performance of the TA-PTO-COF cathode, various types of electrolytes were used for comparison (Fig. S5†). Significantly, the TA-PTO-COF cathode using 2 M ZnSO<sub>4</sub> electrolyte exhibits more competitive capacity and cycling stability compared to the same cathode with other electrolytes (3 M Zn (CF<sub>3</sub>SO<sub>3</sub>)<sub>2</sub>, 3 M Zn (ClO<sub>4</sub>)<sub>2</sub> electrolytes). When 2 M ZnSO<sub>4</sub> was chosen as the electrolyte, the electrochemical performance of TA-PTO-COF was evaluated with the help of cyclic voltammetry (CV) curves at a scan rate of 0.1 mV s<sup>-1</sup> to analyze the redox mechanism of TA-PTO-COF, as presented in Fig. 3a. TA-PTO-COF clearly shows two pairs of redox peaks at 0.71/0.78 V and 0.94/1.05 V, respectively, which can be assigned to the coordination of Zn<sup>2+</sup>/H<sup>+</sup> with C=O and C=N groups in the COF. Importantly, during repeated cycling, the CV curves show a good overlapping characteristic, indicating the outstanding reversibility and chemical stability of the TA-PTO-COF cathode.<sup>49</sup> Furthermore, the galvanostatic charge/discharge profiles display a stable voltage plateau (Fig. 3b), which is consistent with the CV curves. The electrochemical stability of the TA-PTO-COF cathode is significantly improved compared to that of the PTO-NH<sub>2</sub> monomer (Fig. S6†). The corresponding capacity of TA-PTO-COF is 255 mA h g<sup>-1</sup> at 0.1 A g<sup>-1</sup> (Fig. 3c), along with a high initial coulombic efficiency (ICE) of 84%. Even after 100 cycles, a reversible capacity of 176 mA h g<sup>-1</sup> can be maintained. By contrast, when using the PTO-NH<sub>2</sub> monomer as a cathode, only 131 mA h g<sup>-1</sup> was retained. The long-term cycling performance of TA-PTO-COF was evaluated at a current density of 1 A g<sup>-1</sup> (Fig. 3d). After 1000 cycles, a high capacity of 142 mA h g<sup>-1</sup> and a coulombic efficiency of around 100% can be observed. In addition, Fig. 3e

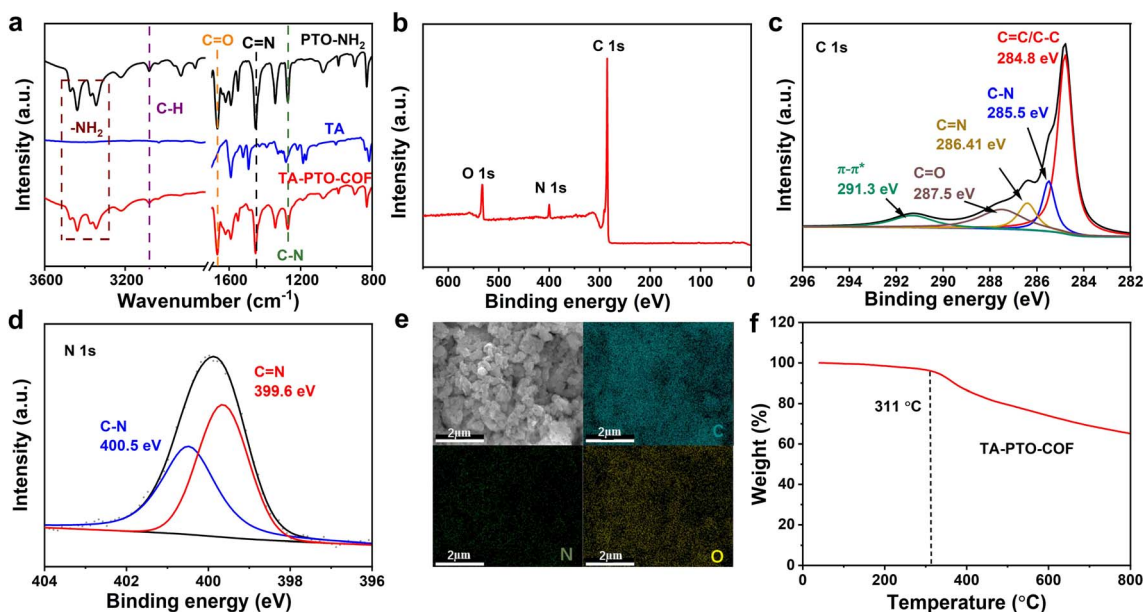


Fig. 2 (a) FT-IR spectra of PTO-NH<sub>2</sub>, TA, and TA-PTO-COF. (b) XPS survey spectrum of TA-PTO-COF. (c) High-resolution C 1s spectrum of TA-PTO-COF. (d) High-resolution N 1s spectrum of TA-PTO-COF. (e) SEM and corresponding elemental C, N, and O mapping. (f) Thermogravimetric analysis of TA-PTO-COF.



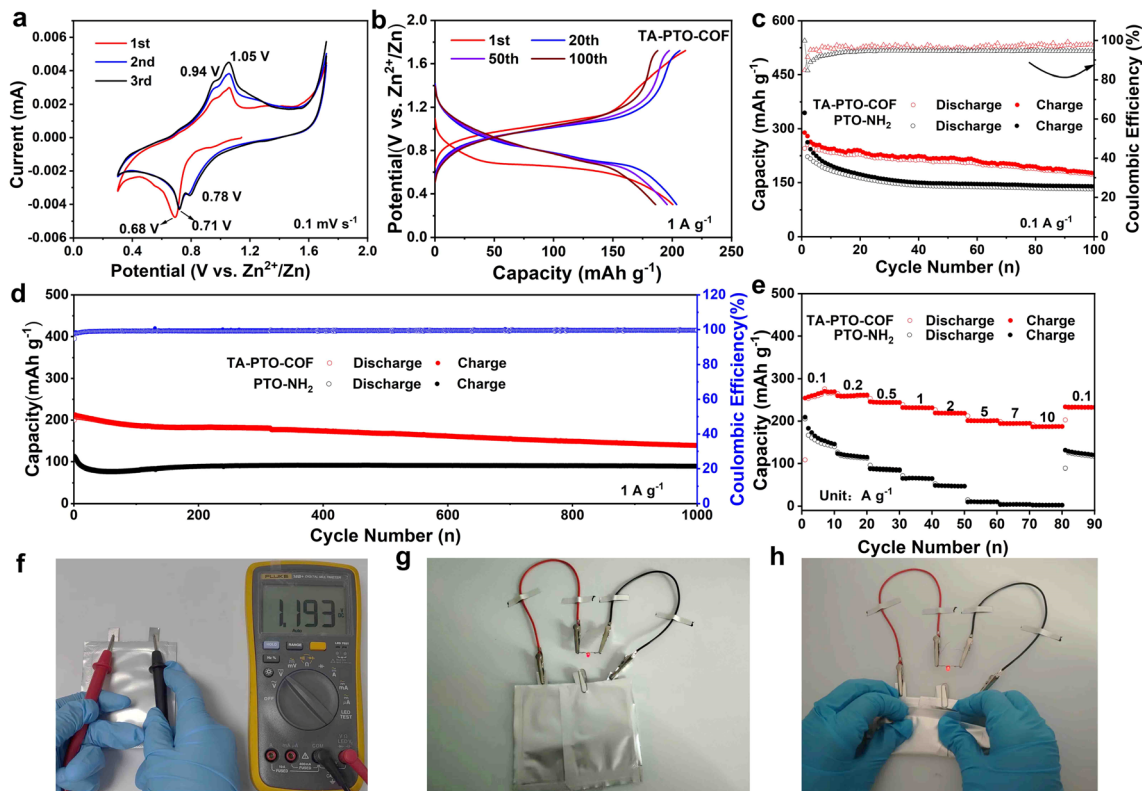


Fig. 3 (a) CV curves of TA-PTO-COF at  $0.1 \text{ mV s}^{-1}$ . (b) Discharge/charge profiles of TA-PTO-COF in  $2 \text{ M ZnSO}_4$  electrolyte at  $1 \text{ A g}^{-1}$ . (c) Cycling stability of TA-PTO-COF and PTO-NH<sub>2</sub> in  $2 \text{ M ZnSO}_4$  electrolyte at  $0.1 \text{ A g}^{-1}$ . (d) Long-duration cycling stability of TA-PTO-COF and PTO-NH<sub>2</sub> in  $2 \text{ M ZnSO}_4$  at  $1 \text{ A g}^{-1}$ . (e) Rate performances of TA-PTO-COF and PTO-NH<sub>2</sub>. (f) Open circuit voltage of a pouch cell. (g and h) Photographs of two pouch cells powering red LEDs under different bending angles.

shows that the rate capability of TA-PTO-COF and the PTO-NH<sub>2</sub> monomer at different current densities ranges from  $0.1$  to  $10 \text{ A g}^{-1}$ . Clearly, TA-PTO-COF exhibits high capabilities of 269, 262, 245, 232, 219, 201, 195, and  $186 \text{ mA h g}^{-1}$  at  $0.1, 0.2, 0.5, 1.0, 2.0, 5.0, 7.0,$  and  $10 \text{ A g}^{-1}$ , respectively. More importantly, when the current density returns to  $0.1 \text{ A g}^{-1}$ , the capacity of TA-PTO-COF returns to its original value, indicating the ideal reversibility and stability. The above results demonstrate that reasonable structural design is conducive to enhancing the electrochemical performance of the organic electrode. The voltage of the pouch cell is shown to be  $1.193 \text{ V}$ . In addition, the pouch cell operates well (lights LED lamps) without deformation or explosion in a folded condition, indicating a high level of safety of the pouch cell (Fig. 3f–h).

To study the reaction kinetics of TA-PTO-COF, electrochemical impedance spectroscopy (EIS), cyclic voltammetry (CV), and the galvanostatic intermittent titration technique (GITT) were carried out. In the EIS plots of PTO-NH<sub>2</sub> and TA-PTO-COF, the charge transfer resistance ( $R_{\text{ct}}$ ) is a concave semicircle in the high-to-middle frequency region. It can be observed that TA-PTO-COF exhibits a smaller charge transfer resistance than PTO-NH<sub>2</sub>, indicating higher electrical conductivity and improved reaction kinetics (Fig. 4a, b). The CV curves of TA-PTO-COF and PTO-NH<sub>2</sub> under  $0.1$ – $1.5 \text{ mV s}^{-1}$  are shown in Fig. 4c and Fig. S7a.† The two pairs of redox peaks and same shape of TA-PTO-COF can be clearly observed in the CV curves at

different scan rates, indicating its excellent electrochemical reversibility and reaction kinetics.<sup>50</sup> Based on the redox peaks and relationship between the peak current ( $i$ ) and scan rate ( $\nu$ ), the  $b$ -value can be calculated to evaluate the electrochemical behavior of TA-PTO-COF and PTO-NH<sub>2</sub>, indicating capacitive behavior ( $b = 0.5$ ) or diffusion controlled behavior ( $b = 1.0$ ). The relationship between  $i$  and  $\nu$  can be described by eqn (1) and (2):<sup>51</sup>

$$i = a\nu^b \quad (1)$$

$$\log(i) = \log(a) + b \log(\nu) \quad (2)$$

The  $b$ -values of TA-PTO-COF were  $0.97, 0.98, 0.97,$  and  $0.98$ , all close to  $1$ , indicating the dominance of capacitive control, which is beneficial to fast redox kinetics (Fig. 4d). In contrast, the  $b$ -values of PTO-NH<sub>2</sub> are  $0.89$  and  $0.86$  (Fig. S7b†). Moreover, the ion diffusion coefficients of the TA-PTO-COF cathode during the charge/discharge processes were calculated using GITT profiles (Fig. 4e) and the following equation:

$$D_{\text{Zn}^{2+}} = \left( \frac{4L^2}{\pi\tau} \right) \times \left( \frac{\Delta E_s}{\Delta E_t} \right)^2 \quad (3)$$

where  $L$  stands for the Zn ion transfer distance and  $\tau$  represents the relaxation time.<sup>52</sup> After calculation, the values of  $D$  at



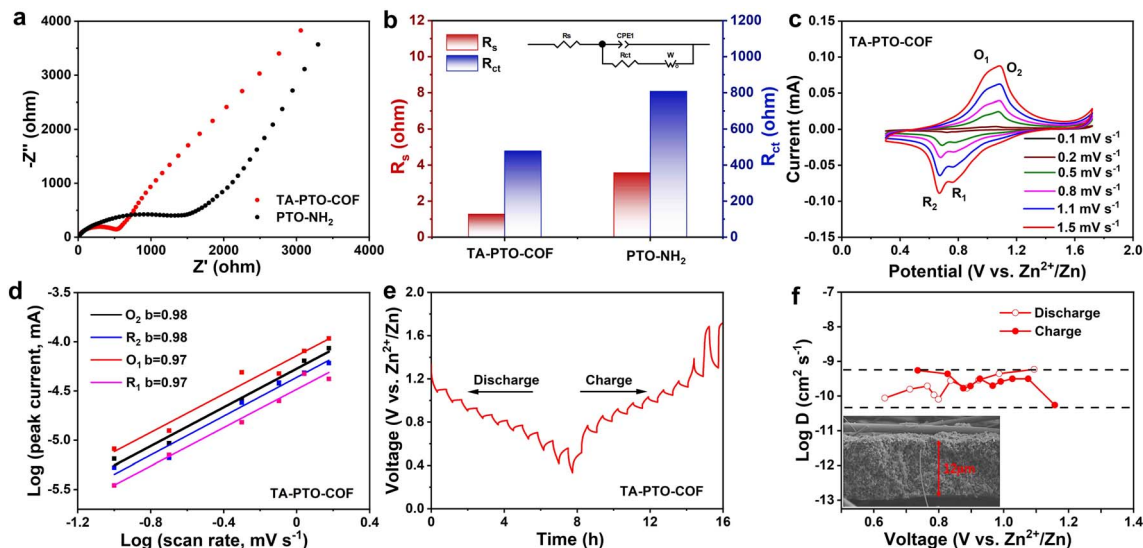


Fig. 4 (a) EIS plots of PTO-NH<sub>2</sub> and TA-PTO-COF. (b) Impedance fitting diagram of PTO-NH<sub>2</sub> and TA-PTO-COF. (c) CV curves of the TA-PTO-COF cathode at various sweep rates. (d) *b* values of TA-PTO-COF. (e) GITT curves of the TA-PTO-COF electrode (first charge/discharge state). (f) Corresponding quantified  $D_{Zn^{2+}}$  at different potential stages and the SEM image of a TA-PTO-COF electrode section.

different states display relatively high and almost constant values ( $8.91 \times 10^{-11}$  to  $5.62 \times 10^{-10} \text{ cm}^2 \text{ s}^{-1}$ ) in Fig. 4f; the high  $D_{Zn^{2+}}$  value is due to the high porosity of TA-PTO-COF which allows internal  $Zn^{2+}$  diffusion.

To deeply reveal the electrochemical storage mechanism of the TA-PTO-COF cathode, *ex situ* FT-IR spectra were recorded. As shown in Fig. 5a and b, in the discharge process, the intensity of the peaks of C=O ( $1660 \text{ cm}^{-1}$ ) and C=N ( $1452 \text{ cm}^{-1}$ ) continuously decreases, indicating that both C=O and C=N are active functional groups in TA-PTO-COF and serve as active sites for  $Zn^{2+}/H^+$  storage. In the subsequent charge process,

these peaks can recover, revealing the excellent reversibility of the TA-PTO-COF cathode material. Meanwhile, *ex situ* XPS spectroscopy was conducted to further analyze the reversible electrochemical process. Fig. 5c shows the high-resolution N 1s spectrum of TA-PTO-COF, which exhibits the C-N (400.5 eV) and C=N (399.6 eV) bonds. When the electrode was discharged to 0.3 V, the peak of C=N bonds shifts slightly toward high binding energy (399.8 eV), accompanied by a reduction in intensity. In contrast, the intensity of the C-N bond gradually increases, primarily due to the consumption of C=N and the formation of C-N. When TA-PTO-COF is charged to 1.72 V, the

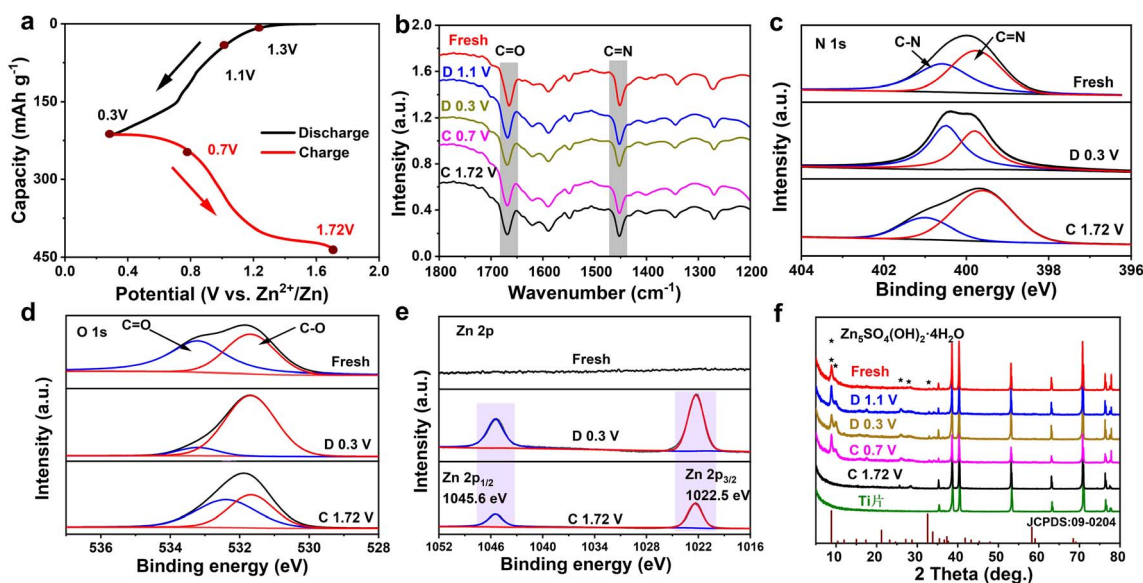


Fig. 5 (a) Charge and discharge profiles of TA-PTO-COF at a current density of  $0.1 \text{ A g}^{-1}$ . (b) *Ex situ* FT-IR spectra of the TA-PTO-COF cathode at different potentials. *Ex situ* XPS analysis of (c) N 1s, (d) O 1s, and (e) Zn 2p. (f) *Ex situ* XRD patterns of the TA-PTO-COF cathode at different potentials.





intensity of the C=N and C–N bonds can be restored. Importantly, a similar process can be observed in the high-resolution O 1s spectrum, where during the discharge process, the intensity of the C=O bond decreases while that of the C–O bond increases (Fig. 5d).<sup>43</sup> Additionally, new peaks at 1022.5 and 1045.6 eV appear, which are attributed to Zn species (Fig. 5e). Afterward, the intensity of these peaks returns to the initial state, suggesting the excellent reversibility of TA-PTO-COF. These evolutions of N 1s, O 1s, and Zn 2p spectra confirm the redox activity of C=N/C=O groups in TA-PTO-COF.

Subsequently, *ex situ* XRD patterns were collected to analyze the storage of Zn<sup>2+</sup>/H<sup>+</sup> during the charge/discharge processes, and the results are presented in Fig. 5f. After discharging to 0.3 V, new diffraction peaks appeared around 8.7°, 10.15°, and 32.57°, which can be ascribed to the Zn<sub>5</sub>SO<sub>4</sub>(OH)<sub>2</sub>·4H<sub>2</sub>O. During the reaction process, the H<sup>+</sup> was embedded in the TA-PTO-COF cathode, resulting in the generation of an equal quantity of OH<sup>−</sup>. Then, the OH<sup>−</sup> ions further reacted with ZnSO<sub>4</sub> and H<sub>2</sub>O, leading to the formation of Zn<sub>5</sub>SO<sub>4</sub>(OH)<sub>2</sub>·4H<sub>2</sub>O. The above results synergistically demonstrate the co-intercalation of Zn<sup>2+</sup> and H<sup>+</sup> in the TA-PTO-COF. In addition, a three-electrode system test was carried out using different electrolytes (2 M ZnSO<sub>4</sub> and 1 M H<sub>2</sub>SO<sub>4</sub>) to further confirm the involvement of H<sup>+</sup> in the charge/discharge processes (Fig. S8†). The working electrode, counter electrode, and reference electrode used were the TA-PTO-COF cathode, platinum sheet, and Ag/AgCl (in saturated potassium chloride), respectively. The obtained CV curve in the 2 M ZnSO<sub>4</sub> electrolyte exhibits two pairs of redox peaks at −0.07/−0.14 V and 0.09/0.19 V.<sup>53</sup> Regarding the 1 M H<sub>2</sub>SO<sub>4</sub> electrolyte, the corresponding CV curve displays a reduction peak at 0.40 V and two oxidation peaks at 0.39/0.57 V. Notably, the CV curves in the 1 M H<sub>2</sub>SO<sub>4</sub> electrolyte overlapped with that in the 2 M ZnSO<sub>4</sub> electrolyte after shifting, confirming the joint participation of H<sup>+</sup> and Zn<sup>2+</sup> in the redox process.<sup>7</sup>

## Conclusions

In summary, a new covalent organic framework with dual redox-active sites was synthesized through a simple condensation reaction of TA and PTO-NH<sub>2</sub> in a Schiff base reaction. The inherent ordered open channel structure, multiple active sites, π–π stacking structure, and high ion/electron conductivity of TA-PTO-COF facilitate fast reaction kinetics and enhance electrochemical performance. When used as the cathode for AZIBs, TA-PTO-COF shows a high capacity of 255 mA h g<sup>−1</sup> at 0.1 A g<sup>−1</sup>. At the same time, the TA-PTO-COF cathode material also shows great rate performance and cycling stability (1000 cycles at 1 A g<sup>−1</sup>). The C=N and C=O bonds in the TA-PTO-COF cathode can reversibly accept/release cations from the electrolyte as determined by *ex situ* FT-IR and XPS tests. This work demonstrates the potential for commercializing organic cathode materials with dual redox active sites in energy storage devices.

## Data availability

The data that support the findings of this study are openly available online.

## Author contributions

H. B. L. and C. F. Z. designed and guided this study. H. B. L., M. G. C., and Z. L. F. carried out the experiments and materials characterization. Q. W. M., L. H. Z., R. W., F. L., and T. F. Z. contributed to the data analysis and co-wrote the paper. C. F. Z. proposed and supervised the project.

## Conflicts of interest

There are no conflicts to declare.

## Acknowledgements

We are thankful for the financial support from the National Natural Science Foundation of China (52172173, 52302205), the Natural Science Foundation of Anhui Province for Distinguished Young Scholars (2108085J25), Excellent Research and Innovation Team Project of Anhui Province (2022AH010001), the Anhui Provincial Natural Science Foundation for Outstanding Young Scholars (2208085Y05), Natural Science Foundation of Anhui Province (2208085QE130), and Distinguished Youth Research Project of Anhui Province (2022AH020013). We also acknowledge the High-performance Computing Platform of Anhui University for providing computing resources.

## Notes and references

- 1 Y. Chen, H. Dai, K. Fan, G. Zhang, M. Tang, Y. Gao, C. Zhang, L. Guan, M. Mao, H. Liu, T. Zhai and C. Wang, *Angew. Chem., Int. Ed.*, 2023, **62**, e202302539.
- 2 M. R. Biradar, A. V. Salkar, P. P. Morajkar, S. V. Bhosale and S. V. Bhosale, *J. Energy Storage*, 2022, **48**, 103953.
- 3 J. Pan, Z. Xia, N. Deng, L. Chen, H. Zhang, Y. Lu, Y. Liu and H. Gao, *Chem. Eng. J.*, 2023, **452**, 138607.
- 4 J. Zhou, S. Zhang, Y.-N. Zhou, W. Tang, J. Yang, C. Peng and Z. Guo, *Electrochem. Energy Rev.*, 2021, **4**, 219–248.
- 5 C. Zhang, R. Yu, T. Zhou, Z. Chen, H. Liu and Z. Guo, *Carbon*, 2014, **72**, 169–175.
- 6 T. Sun, Z. Yi, W. Zhang, Q. Nian, H. J. Fan and Z. Tao, *Adv. Funct. Mater.*, 2023, **33**, 2306675.
- 7 W. Wang, Y. Tang, J. Liu, H. Li, R. Wang, L. Zhang, F. Liang, W. Bai, L. Zhang and C. Zhang, *Chem. Sci.*, 2023, **14**, 9033–9040.
- 8 F. Zhang, M. Wu, X. Wang, Q. Xiang, Y. Wu, J. Ding and Y. Sun, *Chem. Eng. J.*, 2023, **457**, 141335.
- 9 Q. Zhang, Z. Wang, S. Zhang, T. Zhou, J. Mao and Z. Guo, *Electrochem. Energy Rev.*, 2018, **1**, 625–658.
- 10 J. Wang, Y. Lyu, R. Zeng, S. Zhang, K. Davey, J. Mao and Z. Guo, *Energy Environ. Sci.*, 2024, DOI: [10.1039/D3EE02978F](https://doi.org/10.1039/D3EE02978F).
- 11 Z. Liu, R. Wang, Y. Gao, S. Zhang, J. Wan, J. Mao, L. Zhang, H. Li, J. Hao, G. Li, L. Zhang and C. Zhang, *Adv. Funct. Mater.*, 2023, **33**, 2308463.
- 12 N. Dong, F. Zhang and H. Pan, *Chem. Sci.*, 2022, **13**, 8243–8252.
- 13 Y. Chen, J. Li, Q. Zhu, K. Fan, Y. Cao, G. Zhang, C. Zhang, Y. Gao, J. Zou, T. Zhai and C. Wang, *Angew. Chem., Int. Ed.*, 2022, **61**, e202116289.



- 14 Z. Liu, R. Wang, Q. Ma, H. Kang, L. Zhang, T. Zhou and C. Zhang, *Carbon Neutralization*, 2022, **1**, 126–139.
- 15 K. Zhu, C. Guo, W. Gong, Q. Xiao, Y. Yao, K. Davey, Q. Wang, J. Mao, P. Xue and Z. Guo, *Energy Environ. Sci.*, 2023, **16**, 3612–3622.
- 16 T. Kakeya, A. Nakata, H. Arai and Z. Ogumi, *J. Power Sources*, 2018, **407**, 180–184.
- 17 S. Ying, J. Zhou, L. Jin, M. Yemin and H. Xuejie, *Energy Mater.*, 2022, **2**, 200004.
- 18 N. T. H. Luu, A. S. Ivanov, T.-H. Chen, I. Popovs, J.-C. Lee and W. Kaveevivitchai, *J. Mater. Chem. A*, 2022, **10**, 12371–12377.
- 19 R. Zhang, H. Xu, D. Luo, J. Chi, Z. Fan, H. Dou and X. Zhang, *Chem. Eng. J.*, 2023, **458**, 141336.
- 20 G. Li, L. Sun, S. Zhang, C. Zhang, H. Jin, K. Davey, G. Liang, S. Liu, J. Mao and Z. Guo, *Adv. Funct. Mater.*, 2023, **34**, 2301291.
- 21 Z. Sun, Y. Liu, W. Ye, J. Zhang, Y. Wang, Y. Lin, L. Hou, M.-S. Wang and C. Yuan, *Angew. Chem., Int. Ed.*, 2021, **60**, 7180–7187.
- 22 Z. Chen, H. Su, P. Sun, P. Bai, J. Yang, M. Li, Y. Deng, Y. Liu, Y. Geng and Y. Xu, *Proc. Natl. Acad. Sci. U. S. A.*, 2022, **119**, e2116775119.
- 23 H. Li, J. Wu, H. Li, Y. Xu, J. Zheng, Q. Shi, H. Kang, S. Zhao, L. Zhang, R. Wang, S. Xin, T. Zhou and C. Zhang, *Chem. Eng. J.*, 2022, **430**, 132704.
- 24 H. Xun, Z. Chen, Y. Liu, H. Su, J. Yang, Y. Liu and Y. Xu, *ACS Appl. Mater. Interfaces*, 2023, **15**, 29064–29071.
- 25 S. Xu, C. Wang, T. Song, H. Yao, J. Yang, X. Wang, J. Zhu, C.-S. Lee and Q. Zhang, *Adv. Sci.*, 2023, **10**, 2304497.
- 26 P. Xiong, S. Zhang, R. Wang, L. Zhang, Q. Ma, X. Ren, Y. Gao, Z. Wang, Z. Guo and C. Zhang, *Energy Environ. Sci.*, 2023, **16**, 3181–3213.
- 27 J. J. Shea and C. Luo, *ACS Appl. Mater. Interfaces*, 2020, **12**, 5361–5380.
- 28 D. Yao, Y. Zhang, S. Zhang, J. Wan, H. Yu and H. Jin, *J. Mater. Chem. A*, 2023, **11**, 16433–16457.
- 29 C. N. Gannett, J. Kim, D. Tirtariyadi, P. J. Milner and H. D. Abruña, *Chem. Sci.*, 2022, **13**, 9191–9201.
- 30 F. Baskoro, P.-C. Chiang, Y.-C. Lu, J. N. Patricio, S. D. Arco, H.-C. Chen, W.-S. Kuo, L.-L. Lai and H.-J. Yen, *Electrochim. Acta*, 2022, **434**, 141306.
- 31 Y. Zhai, H. Li, Q. Ma, R. Wang, L. Zhang and C. Zhang, *Ionics*, 2023, **29**, 1301–1310.
- 32 Q. Ma, J. Zheng, H. Kang, L. Zhang, Q. Zhang, H. Li, R. Wang, T. Zhou, Q. Chen, A. Liu, H. Li and C. Zhang, *ACS Appl. Mater. Interfaces*, 2021, **13**, 43002–43010.
- 33 J. Xiong, X. Yan, H. Yu, C. Wu, G. Zhao, J. Zhang, Y. Dai, X. Wang, J. Gao, X. Pu, M. Hu, J. Liu and J. Yang, *J. Mater. Chem. A*, 2023, **11**, 8048–8056.
- 34 K. Jia, H. Liu, G. Huang, J. Zhang, X. Liu, L. Li, L. Zhu and F. Wu, *J. Mater. Chem. A*, 2022, **10**, 14917–14922.
- 35 W. Wang, V. S. Kale, Z. Cao, Y. Lei, S. Kandambeth, G. Zou, Y. Zhu, E. Abouhamad, O. Shekha, L. Cavallo, M. Eddaoudi and H. N. Alshareef, *Adv. Mater.*, 2021, **33**, 2103617.
- 36 X. Yang, L. Gong, K. Wang, S. Ma, W. Liu, B. Li, N. Li, H. Pan, X. Chen, H. Wang, J. Liu and J. Jiang, *Adv. Mater.*, 2022, **34**, 2207245.
- 37 D. Ma, H. Zhao, F. Cao, H. Zhao, J. Li, L. Wang and K. Liu, *Chem. Sci.*, 2022, **13**, 2385–2390.
- 38 S. Li, Y. Liu, L. Dai, S. Li, B. Wang, J. Xie and P. Li, *Energy Storage Mater.*, 2022, **48**, 439–446.
- 39 H. Zhao, D. Luo, H. Xu, W. He, B. Ding, H. Dou and X. Zhang, *J. Mater. Sci.*, 2022, **57**, 9980–9991.
- 40 X. Liu, Y. Jin, H. Wang, X. Yang, P. Zhang, K. Wang and J. Jiang, *Adv. Mater.*, 2022, **34**, 2203605.
- 41 H. Gao, A. R. Neale, Q. Zhu, M. Bahri, X. Wang, H. Yang, Y. Xu, R. Clowes, N. D. Browning, M. A. Little, L. J. Hardwick and A. I. Cooper, *J. Am. Chem. Soc.*, 2022, **144**, 9434–9442.
- 42 Y. Lin, H. Cui, C. Liu, R. Li, S. Wang, G. Qu, Z. Wei, Y. Yang, Y. Wang, Z. Tang, H. Li, H. Zhang, C. Zhi and H. Lv, *Angew. Chem., Int. Ed.*, 2023, **62**, e202218745.
- 43 X.-X. Luo, W.-H. Li, H.-J. Liang, H.-X. Zhang, K.-D. Du, X.-T. Wang, X.-F. Liu, J.-P. Zhang and X.-L. Wu, *Angew. Chem., Int. Ed.*, 2022, **61**, e202117661.
- 44 L. Liang, X. Sun, J. Zhang, L. Hou, J. Sun, Y. Liu, S. Wang and C. Yuan, *Adv. Energy Mater.*, 2019, **9**, 1802847.
- 45 M. J. Frisch, G. E. Scuseria, M. A. Robb, J. R. Cheeseman, G. Scalmani, V. Barone, B. Mennucci, G. A. Petersson, H. Nakatsuji, M. Caricato, X. Li, H. P. Hratchian, A. F. Izmaylov, J. Bloino, G. Zheng, J. L. Sonnenberg, M. Hada, M. Ehara, K. Toyota, R. Fukuda, J. Hasegawa, M. Ishida, T. Nakajima, Y. Honda, O. Kitao, H. Nakai, T. Vreven, J. A. Montgomery Jr, J. E. Peralta, F. Ogliaro, M. Bearpark, J. J. Heyd, E. Brothers, K. N. Kudin, V. N. Staroverov, R. Kobayashi, J. Normand, K. Raghavachari, A. Rendell, J. C. Burant, S. S. Iyengar, J. Tomasi, M. Cossi, N. Rega, J. M. Millam, M. Klene, J. E. Knox, J. B. Cross, V. Bakken, C. Adamo, J. Jaramillo, R. Gomperts, R. E. Stratmann, O. Yazyev, A. J. Austin, R. Cammi, C. Pomelli, J. W. Ochterski, R. L. Martin, K. Morokuma, V. G. Zakrzewski, G. A. Voth, P. Salvador, J. J. Dannenberg, S. Dapprich, A. D. Daniels, O. Farkas, J. B. Foresman, J. V. Ortiz, J. Cioslowski and D. J. Fox, *Gaussian 16 revision A.03*, Gaussian, Inc., Wallingford CT, 2016.
- 46 Y. Ma, Y. Wei, W. Han, Y. Tong, A. Song, J. Zhang, H. Li, X. Li and J. Yang, *Angew. Chem., Int. Ed.*, 2023, **62**, e202314259.
- 47 S. Zheng, D. Shi, D. Yan, Q. Wang, T. Sun, T. Ma, L. Li, D. He, Z. Tao and J. Chen, *Angew. Chem., Int. Ed.*, 2022, **61**, e202117511.
- 48 L. Lin, Z. Lin, J. Zhu, K. Wang, W. Wu, T. Qiu and X. Sun, *Energy Environ. Sci.*, 2023, **16**, 89–96.
- 49 Y. Liu, Z. Sun, X. Sun, Y. Lin, K. Tan, J. Sun, L. Liang, L. Hou and C. Yuan, *Angew. Chem., Int. Ed.*, 2020, **59**, 2473–2482.
- 50 L. Zhang, R. Wang, Z. Liu, J. Wan, S. Zhang, S. Wang, K. Hua, X. Liu, X. Zhou, X. Luo, X. Zhang, M. Cao, H. Kang, C. Zhang and Z. Guo, *Adv. Mater.*, 2023, **35**, 2210082.
- 51 Y. Zhang, C. Zhao, Z. Li, Y. Wang, L. Yan, J. Ma and Y. Wang, *Energy Storage Mater.*, 2022, **52**, 386–394.
- 52 S. Wang, Q. Guo, H. Liu, L. Zhang, C. Zhang, T. Zhou, Q. Ma, H. Li, R. Wang and Y. Zheng, *Chem. Sci.*, 2024, **15**, 1051–1060.
- 53 X. Wang, Y. Liu, Z. Wei, J. Hong, H. Liang, M. Song, Y. Zhou and X. Huang, *Adv. Mater.*, 2022, **34**, 2206812.

